Geophys. J. Int. (2009) **177,** 555–570 doi: 10.1111/j.1365-246X.2008.04063.x

Validation of the rupture properties of the 2001 Kunlun, China ($M_s = 8.1$), earthquake from seismological and geological observations

Yi-Ying Wen,[1] Kuo-Fong Ma,[1] Teh-Ru Alex Song,[2]* and Walter D. Mooney[3]

[1] *Graduate Institute of Geophysics, National Central University, Taiwan. E-mail: fong@earth.ncu.edu.tw*
[2] *Seismological Laboratory, California Institute of Technology, USA*
[3] *US Geological Survey, Menlo Park, CA, USA*

Accepted 2008 October 31. Received 2008 October 31; in original form 2008 April 30

SUMMARY

We determine the finite-fault slip distribution of the 2001 Kunlun earthquake ($M_s = 8.1$) by inverting teleseismic waveforms, as constrained by geological and remote sensing field observations. The spatial slip distribution along the 400-km-long fault was divided into five segments in accordance with geological observations. Forward modelling of regional surface waves was performed to estimate the variation of the speed of rupture propagation during faulting. For our modelling, the regional 1-D velocity structure was carefully constructed for each of six regional seismic stations using three events with magnitudes of 5.1–5.4 distributed along the ruptured portion of the Kunlun fault. Our result shows that the average rupture velocity is about 3.6 km s^{-1}, consistent with teleseismic long period wave modelling. The initial rupture was almost purely strike-slip with a rupture velocity of 1.9 km s^{-1}, increasing to 3.5 km s^{-1} in the second fault segment, and reaching a rupture velocity of about 6 km s^{-1} in the third segment and the fourth segment, where the maximum surface offset, with a broad fault zone, was observed. The rupture velocity decelerated to a value of 3.3 km s^{-1} in the fifth and final segment. Coseismic slip on the fault was concentrated between the surface and a depth of about 10 km. We infer that significant variations in rupture velocity and the observed fault segmentation are indicative of variations in strength along the interface of the Kunlun fault, as well as variations in fault geometry.

Key words: Satellite geodesy; Earthquake source observations; Dynamics and mechanics of faulting.

1 INTRODUCTION

The roughly east–west sinistral strike-slip Kunlun fault, one of the faults that accommodates the eastward extrusion of Tibet plateau, is an example of large scale slip partitioning in the continental crust (Tapponnier & Molnar 1997; Meyer *et al*. 1998; Tapponnier *et al*. 2001; Wang *et al*. 2001; Van Der Woerd *et al*. 2002a,b). On 2001 November 14 (09:26:10 GMT), an $M_s = 8.1$ earthquake struck in this active fault zone. According to the US Geological Survey (USGS), the epicentre of the Kunlun earthquake was located in Qinghai Province, northwest China, at 35.946°N and 90.541°E, and the surface rupture extended laterally more than 400 km (Lin *et al*. 2002, 2003; Xu *et al*. 2002; Van Der Woerd *et al*. 2002a) (Fig. 1). Since 1937, several large ($M > 7$) earthquakes have occurred along different segments of the Kunlun fault (Fig. 1): the 1937 $M = 7.5$ Huashi Canyon earthquake, the 1963 $M_s = 7.1$ Dulan earthquake, the 1973 $M_s = 7.3$ Manyi earthquake and the 1997 $M_w = 7.5$ Manyi earthquake. The surface rupture of all the events are believed to have been greater than 150 km, and the focal mechanisms all show distinct left-lateral strike-slip motion (Molnar & Deng 1984; Gu *et al*. 1989). The ruptured segment of the 2001 Kunlun earthquake lies between the four previous large events. Seismicity that was recorded 1 yr before the 2001 Kunlun earthquake by the China Seismic Network DMC (CSNDMC) indicated that there was almost no activity in the rupture area of the 2001 event. The locations of aftershocks in the first year following the main shock were concentrated on the eastern end of the ruptured fault, with depths reaching nearly 35 km (Fig. 1). Similar to previous large historical events that occurred along the Kunlun fault, the 2001 Kunlun earthquake showed a distinct left-lateral strike-slip motion according to the Harvard CMT solution.

Fig. 1 also shows the epicentres and focal mechanisms determined by various institutes, namely, USGS, Earthquake Research

*Now at: Department of Terrestrial Magnetism, Carnegie Institution of Washington, Washington, DC, USA.

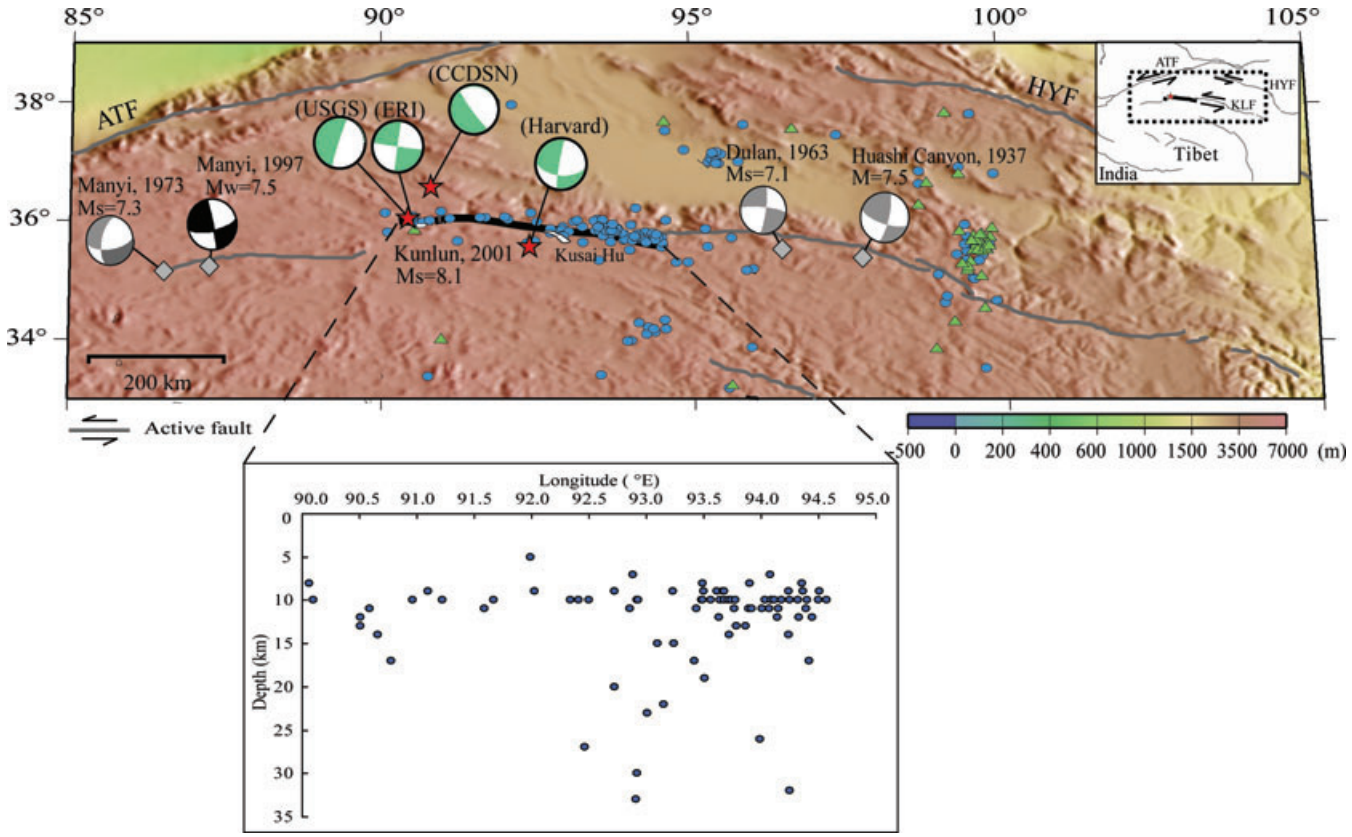

Figure 1. Locations (asterisks) and fault plane solutions (green beach balls) of the 2001 Kunlun earthquake determined by USGS, ERI, CCDSN and HARVARD, respectively. The diamonds indicate the locations of historic large events along the Kunlun fault: the 1937 M7.5 Huashi Canyon earthquake, the 1963 M_s7.1 Dulan earthquake, the 1973 M_s7.3 Manyi earthquake, and the 1997 M_w7.5 Manyi earthquake, with the focal mechanism in black from the Harvard CMT solution, and the grey ones from Molnar & Deng (1984). The thick black line represents the surface rupture during the main shock. The triangles and circles show the foreshocks and aftershocks, recorded by CSNDMC, within 1 yr before and after the main shock, respectively. The lower panel shows the depth distribution of aftershocks near the ruptured fault. The inset map at the right upper corner shows the major faults around Tibet, and the dashed rectangle indicates the region of the Kunlun fault. KLF, Kunlun fault; ATF, Altyn Tagh fault and HYF, Haiyuan fault.

Institute in Tokyo (ERI), China Center of Digital Seismic Network (CCDSN) and Harvard CMT. The fault plane solution of ERI and Harvard CMT are similar, with almost east–west strike-slip focal mechanisms, in agreement with the strike direction of the Kunlun fault. The reported hypocentres for the main shock are all located close to the western terminus of the ruptured fault, while the centroidal solution determined by the Harvard CMT is located near the middle of the rupture fault. The hypocentral location exhibits the initial point of fault rupture, while the centroidal solution corresponds to the region of maximum energy release. In our study, we use the USGS hypocentre, which had been carefully relocated, and has been widely adopted in previous works (Bouchon & Vallée 2003; Lin *et al*. 2003; Antolik *et al*. 2004). The fact that the hypocentre is located at the western end of the rupture suggests an almost unilateral rupture of the earthquake.

Post-earthquake geological field investigations were carried out by four groups, as reported by Lin *et al*. (2002), Xu *et al*. (2002, 2006), Li *et al*. (2005) and Klinger *et al*. (2005). All studies have revealed significant left-lateral slip along the Kunlun fault, but the estimated maximum slips of 16.3 and ∼8 m are very different (Fig. 2). To resolve this discrepancy in maximum slip for the 2001 Kunlun earthquake, Xu *et al*. (2006) re-investigated several sites where the maximum slip of 16.3 m was reported by Lin *et al*. (2002). They concluded that the reported maximum slip of 16.3 m almost certainly represents the cumulative slip of several similar historical events, and report a maximum slip of about 7.6 m (+/– 0.4 m). The surface slip along the ruptured fault defined from InSAR data (Lasserre *et al*. 2005) or measured at high resolution using optical correlation of satellite images (Klinger *et al*. 2006) are consistent with the observations of Xu *et al*. (2006), as shown in Fig. 2. Regardless of the precise amount of the maximum slip, the investigations all showed maximum slip at a location 240–280 km to the east of the epicentre. The surface rupture consists of shear, transtensional, transpressional, extensional and thrusting fractures, as well as tension gashes, pull-aparts, releasing or compressing jogs and mole tracks (Lin *et al*. 2002, 2003; Xu *et al*. 2002, 2006; Van Der Woerd *et al*. 2002a; Li *et al*. 2005). Reverse components of slip are also observed, but they are much smaller than the horizontal slip at the same locations (Xu *et al*. 2002, 2006).

In addition to significant variations in the magnitude of slip along the 2001 rupture, a large variation in rupture velocity has been reported. Bouchon & Vallée (2003) used regional surface wave data to determine a rupture velocity of ∼5.0 km s^{-1}, greatly exceeding the shear wave velocity, for most sections of the fault. However, Hjorleifsdottir *et al*. (2003) modelled long-period body waves and concluded that the average rupture velocity proposed by Bouchon & Vallée (2003) was likely too high. On the other hand, Robinson *et al*. (2006) obtained a rupture velocity that even exceeded the *P*-wave velocity in the region of highest slip. Recently, Tocheport

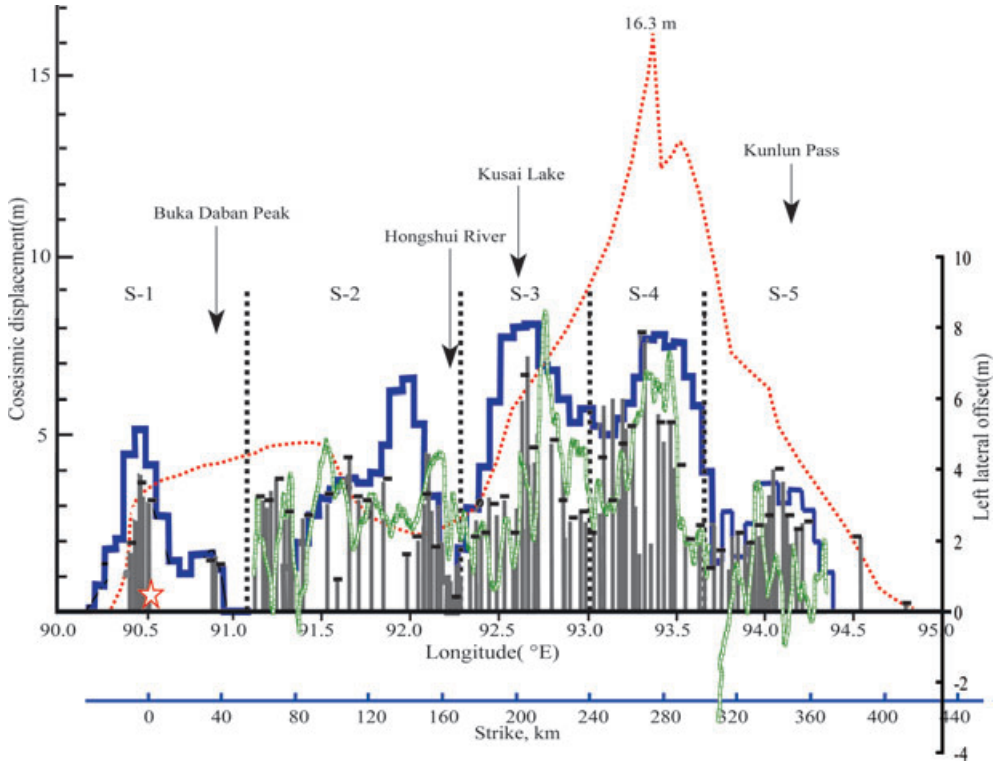

Figure 2. Coseismic horizontal displacements from field investigation and InSAR data. The red dashed line indicates the field data modified from Lin *et al*. (2003); note that the maximum estimated slip of 16.3 m was not confirmed by the later field study of Xu *et al*. (2006). The grey bars indicate the field measurements of Xu *et al*. (2006), and the blue line represents the coseismic horizontal displacements modelled from InSAR data of Lasserre *et al*. (2005). The green line indicates measured left lateral offsets of Klinger *et al*. (2006). The red asterisk indicates the epicentre. The fault ruptures were classified into five segments as S-1 to S-5, shown by vertical dashed lines, according to Xu *et al*. (2006). The black bars represent the average offset of each 5 km grid. The distance to the strike of the fault from the epicentre was shown in scale.

et al. (2006) tested the influence of the maximum allowed rupture velocity during slip inversion and suggested a maximum average rupture velocity of 3.5 km s^{-1}. Other studies using teleseismic body waves also found a similar mean rupture velocity of 3.4 km s^{-1} (Lin *et al*. 2003; Ozacar & Beck 2004) and 3.6 km s^{-1} (Antolik *et al*. 2004). Notably, their inversion did not require supershear rupture velocity to improve the waveform fitting. However, they found that teleseismic body waves are less sensitive to the rupture velocity than regional surface waves because teleseismic body waves left the source with a nearly vertical departure angle (Tocheport *et al*. 2006).

In previous studies, model results were obtained either from teleseismic body waves or regional surface waves alone. In this study, we utilize most of the available data and break down the non-linearity in the modelling by introducing an iterated approach, with successive additions of surface waves, which are much more sensitive to the rupture velocity than the body waves, in order to validate models of the rupture velocity of the 2001 Kunlun earthquake. First, we use the teleseismic body wave waveforms, together with the field observations of fault slip, for an inversion for the spatial slip distribution, assuming a uniform rupture velocity (3.4 km s^{-1}). Then, to evaluate the actual rupture velocity model, we use our spatial slip distribution to forward model regional surface waves, since these have a relatively low phase velocity and are very sensitive to variations in the rupture velocity along the fault. In the forward modelling of the regional surface waves, the detailed regional velocity structure around the Kunlun fault and regional seismic stations were examined from three smaller events located along the Kunlun fault, instead of one event near the epicentre (Bouchon & Vallée 2003). The regional surface wave modelling with a realistic slip distribution (obtained from teleseismic body wave inversion) shows that the rupture velocity largely varies from a low value of about 2 km s^{-1} to a maximum value of about 6 km s^{-1}, with an average rupture velocity of 3.6 km s^{-1}.

2 SPATIAL SLIP DISTRIBUTION FROM TELESEISMIC WAVEFORMS

2.1 Data, fault geometry and methods

We use teleseismic broad-band waveforms for both *P* and *S* waves from the IRIS stations with epicentral distances between 30° and 90° in the inversion for the spatial slip distribution. The teleseismic Green's functions were computed by the generalized ray theory method (Langston & Helmberger 1975). To model the earthquake rupture process, we consider waveforms with duration of 130 s. This duration provides waveforms that exhibit strong similarities for the stations considered. We modelled the waveforms from 10 s before to 130 s after the *P*- and *S*-wave arrivals, with a sampling rate of 0.5 s. We eliminated the stations for which unmodelled phases, such as PP, SS and ScS phases, arrived during the 130 s rupture-duration time window. According to the empirical velocity model of IASP91, for a 15-km-deep source, the stations with an epicentre distance greater than 55° would not have any influence from the PP phase but only from the small PcP phase, and the stations between

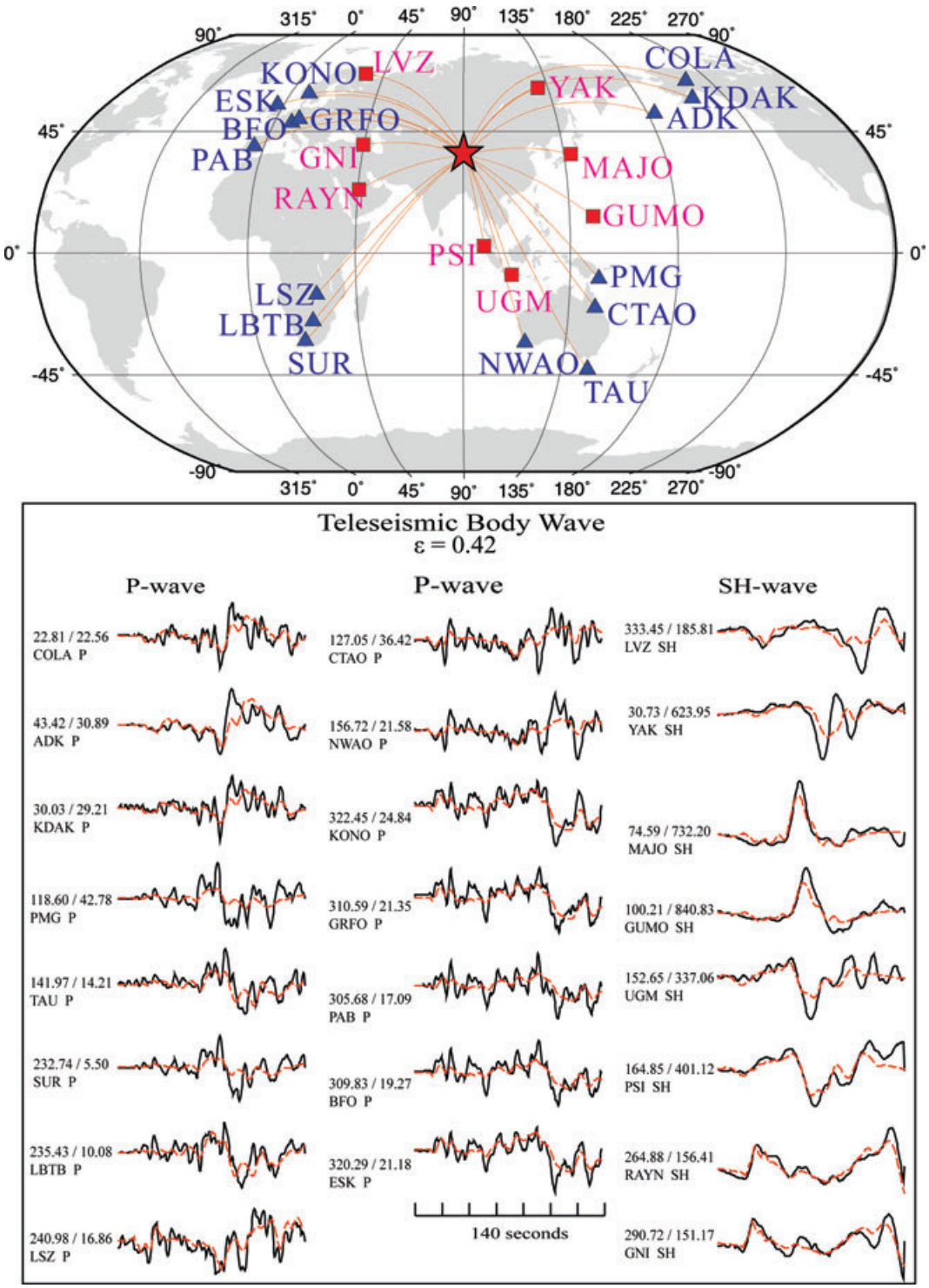

Figure 3. The station distribution and comparison of the observed (solid line) and the synthetic (dashed line) waveforms from the model of Fig. 6(d). The asterisk indicates the epicentre of the 2001 Kunlun earthquake. The triangles and squares indicate the stations for *P*-wave and SH-wave waveforms, respectively, used in this study. In total, 23 waveforms were used. The numbers above the station code denote the station azimuth in degree and peak value of the record in micrometres.

35° and 55° would not have any contributions from either the SS or ScS phases. By these criteria, we considered the vertical component for 15 stations for *P*-wave modelling and the transverse component for 8 stations for SH-wave modelling for the finite-fault modelling (Fig. 3). This combination of phases provides a good azimuthal coverage of the earthquake. We removed the instrument response from the original waveforms, integrated the records into the displacement, and bandpass filtered the data from 0.01 to 0.5 Hz.

The geometry of the main surface rupture of the 2001 Kunlun earthquake is nearly linear, closely follows a pre-existing active fault

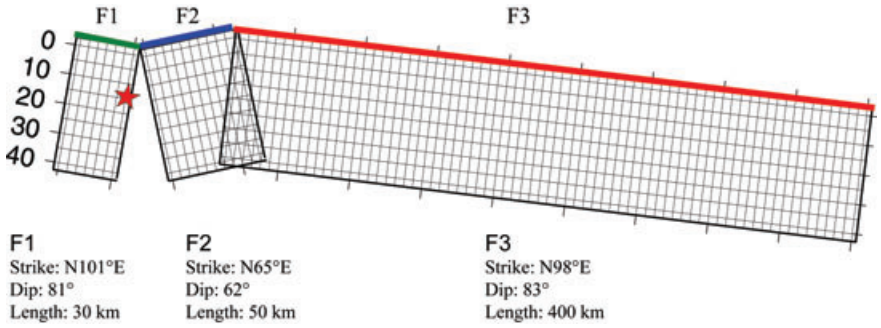

Figure 4. The fault geometry determined from geological field observations (Xu *et al.* 2002, 2006; Van Der Woerd *et al*. 2002a,b) consisting of three fault segments with different strikes, with fault lengths of: (F1) 30 km to the west; (F2) 50 km in the middle and (F3) 400 km to the east. The asterisk indicates the hypocentre. The grid size is 5 km × 5 km.

(Van Der Woerd *et al*. 2002b; Lin *et al*. 2003), and has a strike of N90–110°E (Xu *et al*. 2006). The surface rupture, which has been mapped in the field, includes near the western end a 40-km-long extensional step-over graben system that separates two strike-slip segments: (1) a 30-km-long segment to the west and (2) a 350-km-long segment to the east (Klinger *et al*. 2005, 2006; Lasserre *et al*. 2005; Xu *et al*. 2006). Ozacar & Beck (2004), Antolik *et al*. (2004) and Tocheport *et al*. (2006) have addressed the consequences of this complex stepover geometry on the observed waveforms. Based on the above field observations and the models derived from seismological data, we propose a fault model with the following geometry: (1) a 30 km fault segment to the west of the epicentre oriented N101°E, and dipping 81°, (2) a 50 km fault segment to the east of the epicentre oriented N65°E, and dipping 62° and (3) a third 400-km-long segment, consisting of the rest of the fault, oriented N98°E, and dipping 83° (Fig. 4).

For the purpose of modelling, each fault segment is treated as a planar rupture surface, with a width (i.e. downdip extent) of 40 km (Fig. 4). The fault is then divided into finite subfaults, each with a dimension of 5 km × 5 km in the strike and dip directions. The source–time function is a triangle with a width of 3 s. To allow for a variation in rake angle, a point source with dip-slip and strike-slip components, respectively, was considered in the middle of each subfault for the Green's function calculation. For a given station, the displacement record can be represented as the linear sum of slips contributed from each subfault with appropriate time delays due to the rupture velocity and propagation traveltimes.

Crustal thickness has been variously estimated to increase from ∼50 km near the northern edge of Tibetan plateau to as much as ∼80 km around the Qang Tang block (Galvé *et al*. 2002; Vergne *et al*. 2002). Wittlinger *et al*. (2004) report a maximum crustal thickness of ∼90 km under the western Qang Tang, a result that has not been confirmed by other measurements (Zhao *et al*. 2005; Li *et al*. 2006). The Kunlun fault represents the northern boundary of the plateau proper, and the Moho depth increases from 62 km depth on the northern side to 72 km on the southern side (Galvé *et al*. 2002). Waves propagating to the south across the Tibetan plateau are strongly influenced by the thicker crust. Thus, two crustal velocity structures, corresponding to stations to the north and south of the Kunlun fault, were used in the calculation of Green's functions. The southern velocity structure has a crustal thickness of 72 km, while, to the north, the crustal thickness is 62 km, as modified from Galvé *et al*. (2002; Fig. 5).

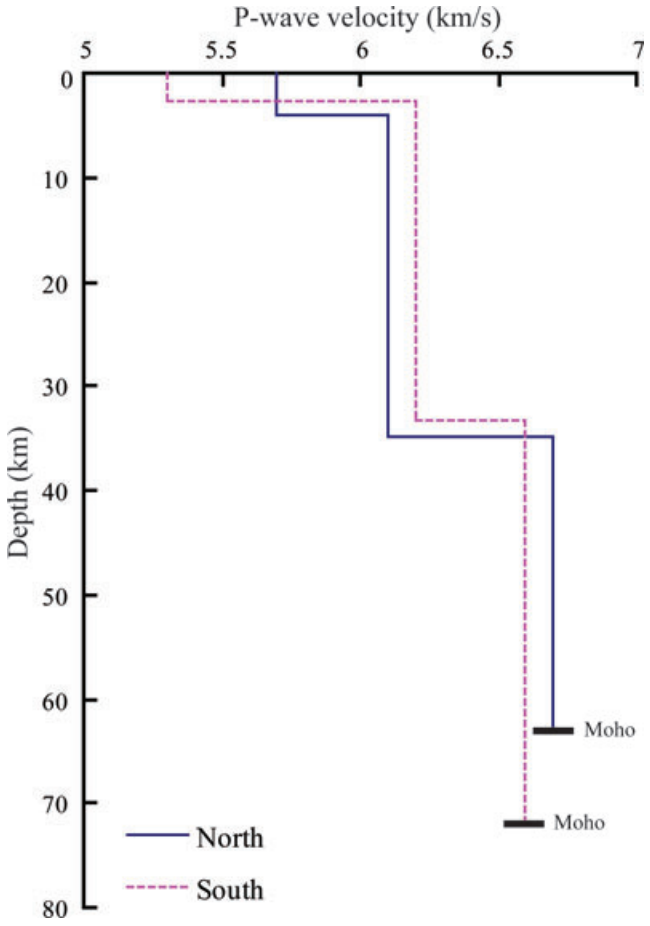

Figure 5. The 1-D velocity structure used for the calculation of teleseismic Green's functions (modified from Galvé *et al*. 2002). The solid and dashed lines represent the structure for the stations to the north and south of the Kunlun fault, respectively.

The observed and synthetic waveforms are represented as a system of linear equations:

$$\mathbf{Ax} = \mathbf{b}, \tag{1}$$

where $\boldsymbol{A}$ is the matrix of Green's functions, $\mathbf{b}$ is the observed waveform data vector and $\mathbf{x}$ is the solution matrix of the subfault

dislocation. The error is defined as:

$$\varepsilon = (\mathbf{Ax} - \mathbf{b})^2 / \mathbf{b}^2. \quad (2)$$

2.2 Results of modelling the composite fault, with additional constraints from geological and remote sensing observations

Fig. 6 shows our inverted slip distribution comparing with the earlier results of Lin *et al*. (2003), Antolik *et al*. (2004) and Ozacar & Beck (2004). The slip distributions are aligned at the epicentre for comparison. The results are generally consistent, particularly for the large slips located about 200–260 km to the east of the epicentre. Our results show relatively less slip, about 4 m near the surface, as compared to others. The comparison of the synthetic and observed waveforms is shown in Fig. 3. We consider a constant rupture velocity of 3.4 km s^{-1} for the inversion. The seismic moment we obtained for this model is 4.9 $\times$ 10^{27} dyne-cm (M_w = 7.7), slightly less than the value of 5.9 $\times$ 10^{27} dyne-cm (M_w = 7.8) reported by Harvard CMT solution.

The remote sensing images provide more continuous geological constraints on slip than localized field studies. We note that the field observations of Xu *et al*. (2006) are quite consistent with the geodetic studies reported by Lasserre *et al*. (2005) and Klinger *et al*. (2005, 2006), as delineated in Fig. 2. We therefore feel confident in using the field observations of Xu *et al*. (2006) as primary constraints on the surface slip in our seismic inversion. We averaged the surface slips of Xu *et al*. (2006) within the corresponding 5 km grid in the finite-fault model (Fig. 2) and added these values to the bottom of the observed waveform data **b** vector. When the observed surface slip was taken as a constraint in the full inversion, the calculated spatial slips are in good agreement with the observed surface slip. Our final spatial slip distribution can explain 97 per cent of the observed surface slips. By introducing the field observations, our inverted slip model had the important constraints of the actual measured surface slips. In addition, we applied a seismic moment constraint in the inversion so that the total seismic moment is consistent with that determined by the Harvard CMT solution. Figs 7(a) and 8(a) show the inverted spatial slip distributions as constrained by the geological data of Xu *et al*. (2006) and Klinger *et al*. (2006), respectively. The corresponding waveform fits are shown in Figs 7(b) and 8(b), respectively. The slip patterns and waveforms are fairly similar due to the consistency in the surface slip distributions of Xu *et al*. (2006) and Klinger *et al*. (2006). In view of the consistency, we adopt the Xu *et al*. (2006) spatial slip distribution, as shown in Fig. 7(a) in our further calculations.

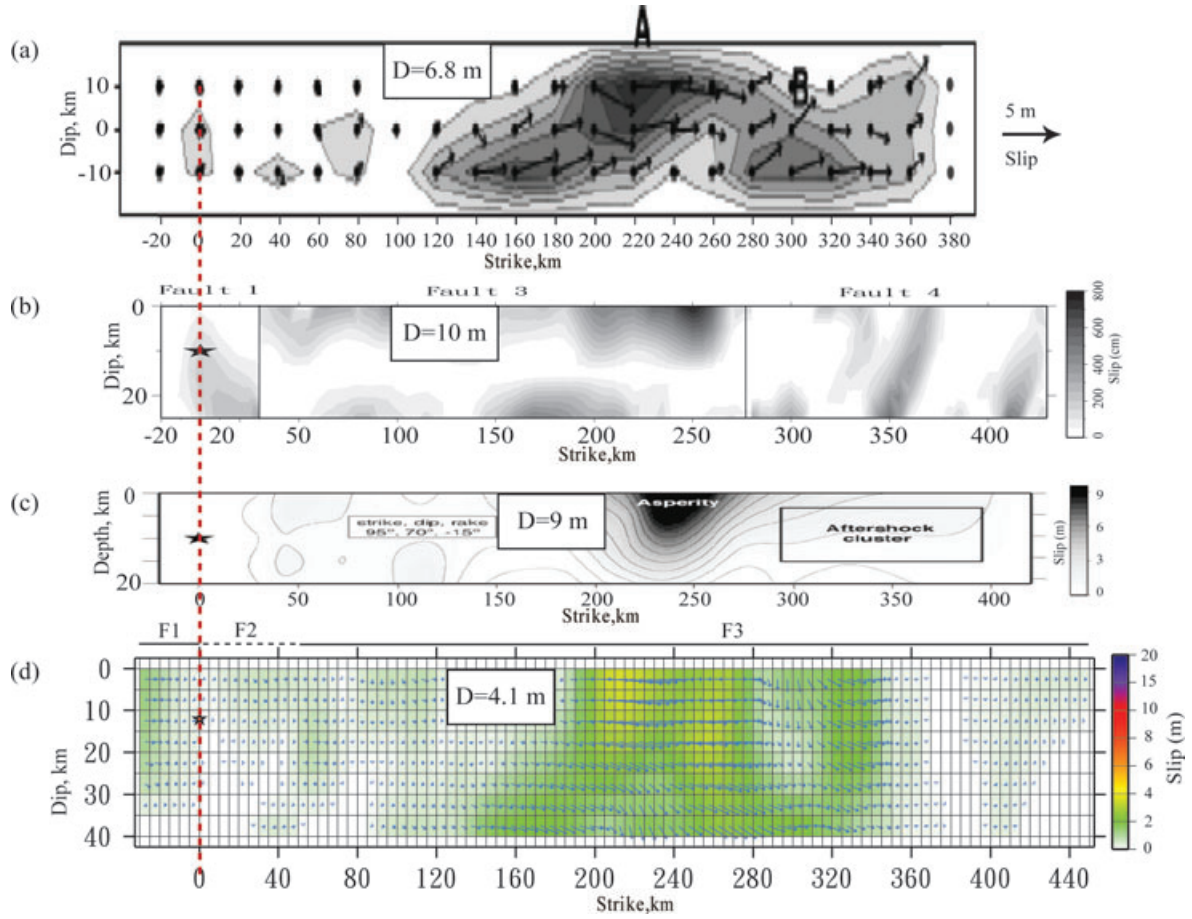

Figure 6. Comparison of slip distributions from (a) Lin *et al*. (2003), (b) Antolik *et al*. (2004), (c) Ozacar & Beck (2004) and (d) our preliminary result. The asterisk represents the hypocentre, which is aligned on the vertical dashed line. The arrows in the top and bottom panels, (a) and (d), indicate the slip vectors on the rupture plane for Lin *et al*. (2003) and our model. Slip is indicated in panels (b) and (c) by the shaded contours. The parameter *D* is maximum slip on fault. All models are in good agreement regarding the location of the main slip, which is more than 200 km east of the hypocentre.

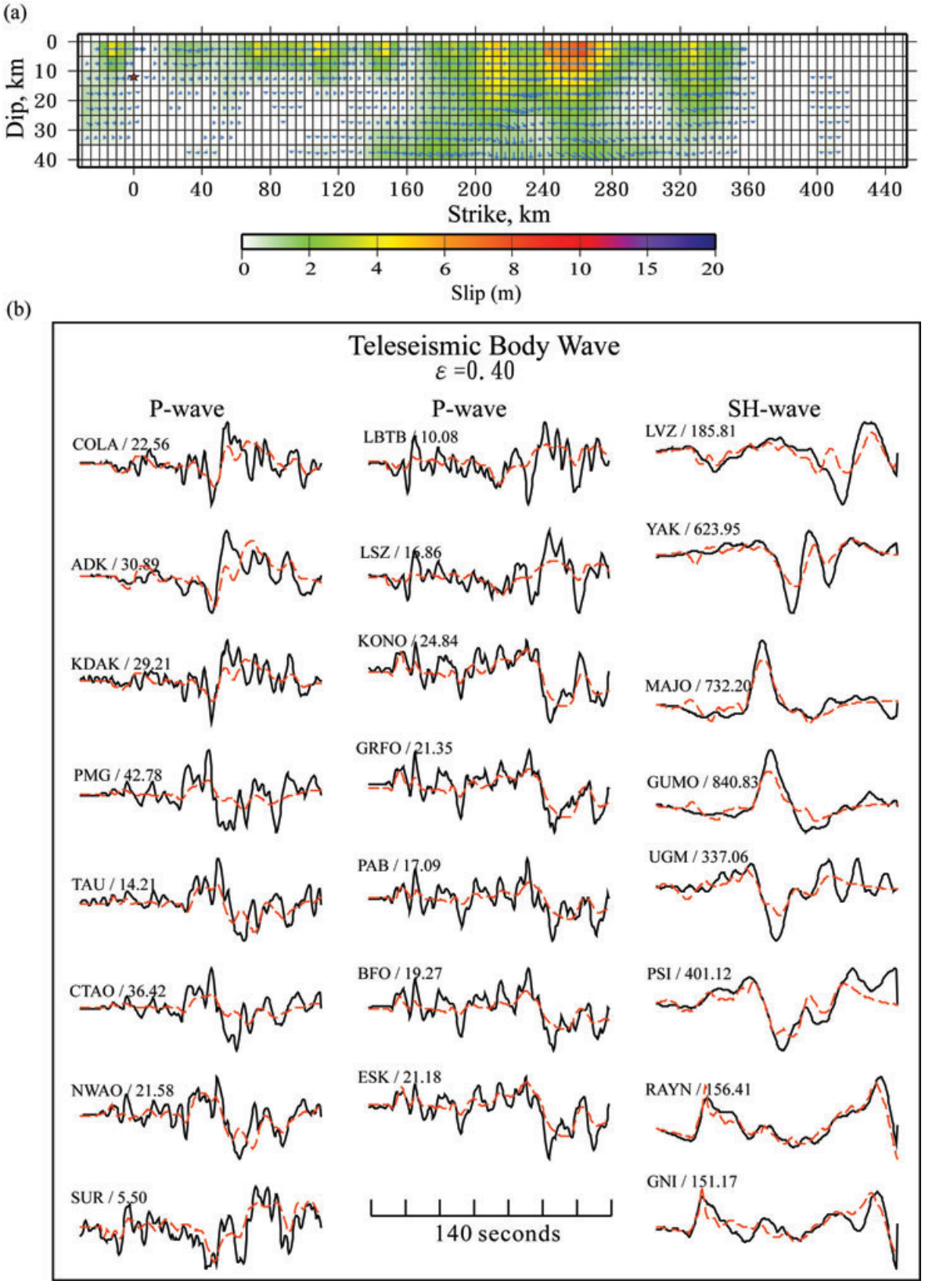

Figure 7. (a) Inverted spatial slip distribution from teleseismic data using the geological constraints of Xu *et al*. (2006), and (b) comparison of the observed (solid line) and the synthetic (dashed line) waveforms. The amount of slip (metres) is indicated by the colour bar. The asterisk indicates the hypocentral location. The arrow indicates the slip vector on the rupture plane. The station name and peak value of the record in micrometres are shown above the waveforms.

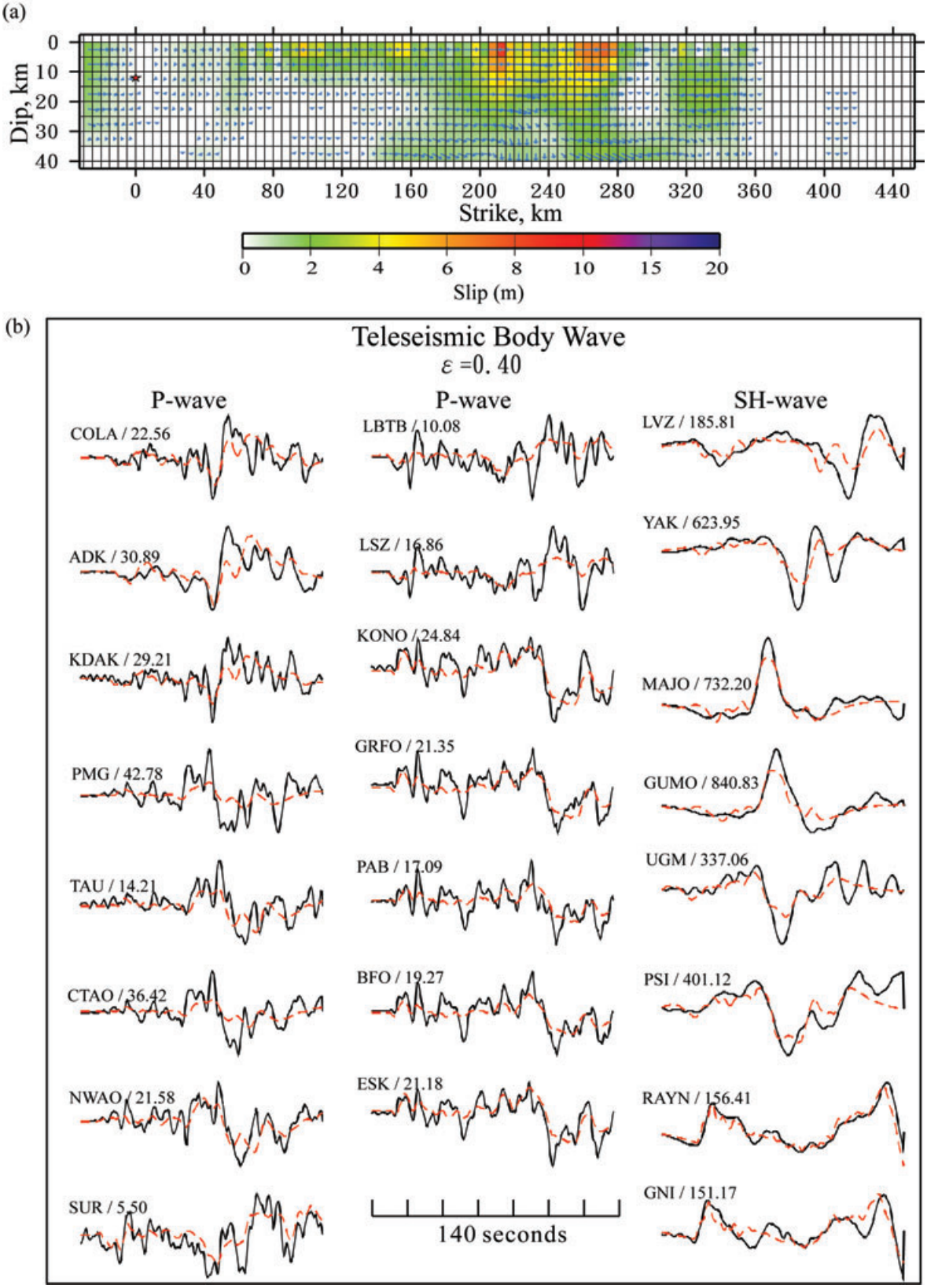

Figure 8. (a) Inverted spatial slip distribution from teleseismic data using the surface slip constraints of Klinger *et al*. (2006), and (b) comparison of the observed (solid line) and the synthetic (dashed line) waveforms. The amount of slip (metres) is indicated by the colour bar. The asterisk indicates the hypocentral location. The arrows indicate the slip vectors on the rupture plane. The station name and peak value of the record in micrometres are shown above the waveforms.

3 VALIDATION ON RUPTURE VELOCITY FROM REGIONAL SURFACE WAVES

3.1 Refined regional velocity structure

The rupture velocity (Vr) is usually considered to be ∼0.7–0.9 times the shear wave velocity (c_S). However, as mentioned earlier, recent studies indicate that the 2001 Kunlun earthquake might have ruptured at a supershear-wave velocity. This was first suggested by Bouchon & Vallée (2003), who analysed regional surface waves and obtained a supershear rupture speed, with an average value of 3.9 km s^{-1} (which exceeds the shear wave velocity of the brittle part of the crust) and a maximum rupture speed of about 5.0 km s^{-1} for 300 km. However, analysis of SH body waves by Robinson *et al*. (2006) suggests that the rupture speed (∼6.7 km s^{-1}) exceeds even the *P*-wave speed (c_P) in the brittle upper crust. We seek to validate these reported variations of rupture speed by forward modelling of the regional surface waves, and using our spatial slip distribution that was obtained from the teleseismic waveforms.

Table 1. Earthquake parameters of the three smaller events used for the refinement of 1-D regional velocity structure. The epicentre was determined by CSNDMC. The nodal plane was determined by the Harvard CMT solution.

	2000/11/26	2002/10/19	2002/10/26
Epicentre	90.530°E 35.821°N	92.923°E 35.744°N	95.961°E 35.189°N
Depth	32 km	30 km	31 km
Nodal Plane 1	298/38/14	186/76/−166	11/78/176
M_w	5.4	5.1	5.4

We considered six regional stations, as used by Bouchon & Vallée (2003) (Fig. 9), in our forward modelling. For the 400-km-long fault rupture of the 2001 Kunlun earthquake, a careful examination of regional 1-D velocity structures between the fault and the regional stations are necessary to minimize the introduction of wave propagation artefacts into the synthetic waveforms. We removed the instrument response from the original waveforms, integrated the records into the displacement, and bandpass filtered the data from

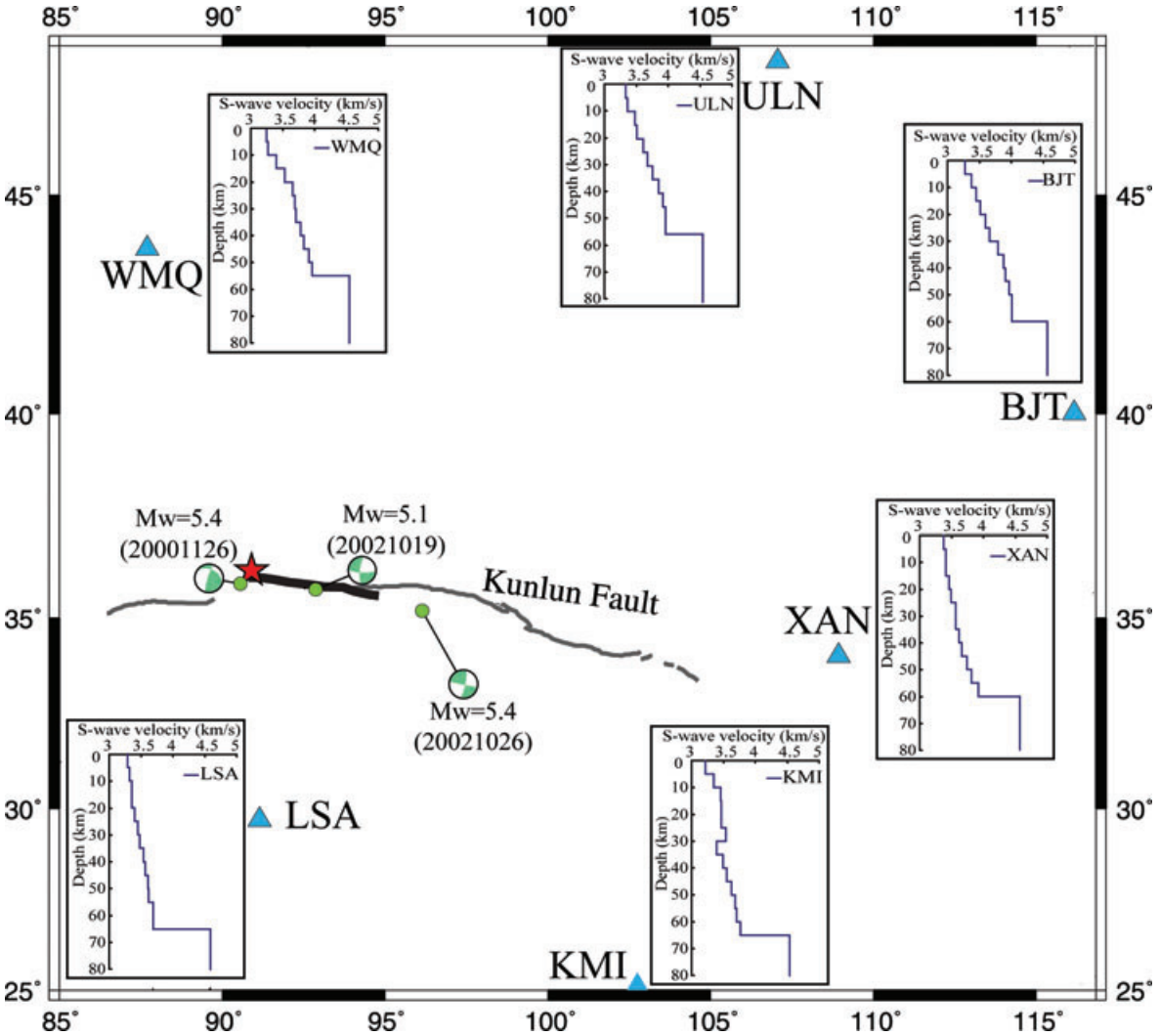

Figure 9. The distribution of the three smaller events (dots) from Chinese CSNDMC earthquake network with focal mechanisms from Havard CMT used to model the 1-D regional crustal velocity structure. The regional stations (triangles) and the 1-D *S*-wave velocity structure, modified from Bouchon and Vallée (2003), for each station are also shown. The thick black line shows the trend of the surface rupture of the 2001 Kunlun earthquake, and the asterisk indicates the epicentre of 2001 Kunlun main shock.

0.008 to 0.05 Hz. We used a frequency–wavenumber (*F–K*) integration method (Zhu & Rivera 2002) to compute the synthetic regional surface waveforms. By examining the available surface waves at these six stations, we refined the regional 1-D velocity structure based on three earthquakes with magnitudes of 5.1–5.4 distributed generally to the west, middle and east of the ruptured fault (Fig. 9). The source parameters for these three events are listed in Table 1. Fig. 9 shows the refined velocity structure determined for the regional stations. In general, the regional velocity structure we derived has slightly lower velocities and a thicker crust than those used by Bouchon & Vallée (2003). Specifically, our velocity structure has a thicker (65 km) crust south of the Kunlun fault, and a

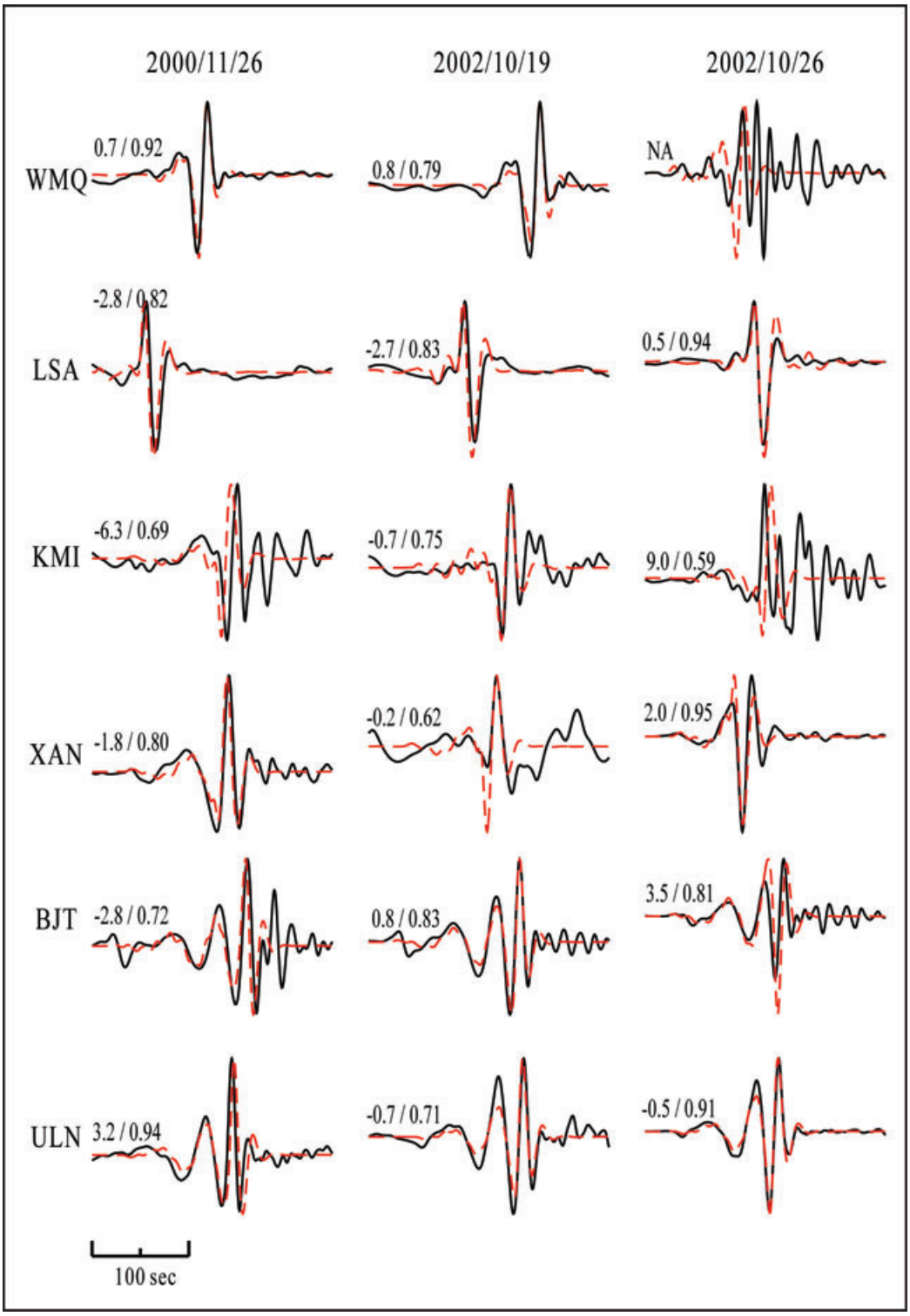

Figure 10. The comparison of the observed (solid line) and the synthetic (dashed line) regional surface waveforms of the three smaller events using the refined 1-D velocity structure (see text). All waveforms are normalized. The numbers separated by a slash above the waveform denote: (1) the time delay of the peak pulse as measured between the synthetic waveform and data record in seconds and (2) the cross-correlation coefficient of the synthetic and observed data.

thinner (55 km) crust to the north. Fig. 10 shows the comparison of the synthetics to the observed regional surface waves for the three selected earthquakes. The delay time and the corresponding cross correlation of the synthetics to the observations are also shown for each of the three selected events.

3.2 Determination of the rupture velocities

We now forward model the regional surface wave using: (1) our refined 1-D velocity models; (2) our derived spatial slip model which was assumed a constant rupture speed of 3.4 km s^{-1} (Fig. 7a). The Green's function for regional surface waves was computed for a point source in the middle of each subfault. The synthetic waveform then can be represented as the linear sum:

$$\mathbf{S} = \boldsymbol{A}_s \boldsymbol{x}_\mathrm{m}, \tag{3}$$

where **S** is the synthetic regional surface waveform vector, $\boldsymbol{A}_\mathrm{s}$ is the matrix of Green's function of regional surface wave and $\mathbf{x}_\mathrm{m}$ is the solution matrix derived from teleseismic waveform inversion.

Fig. 11 shows a comparison of the initial synthetic and observed surface waveforms corresponding to uniform speed (3.4 km s^{-1}) slip model. We calculate the misfit of synthetic to the observed regional surface waves, denoted as $\boldsymbol{\varepsilon}_\mathrm{sur}$, using the same definition as used for teleseismic data. The comparison for our initial model with a constant rupture velocity is not satisfactory, with a value of $\boldsymbol{\varepsilon}_\mathrm{sur}$ of 1.02. The misfit is especially notable in the amplitudes of the surface waves, and we find an average time shift of 2.8 s. In view of the misfit in amplitudes and arrival times, we must consider a more realistic variation in the rupture velocity during the large (410 km) fault model. Therefore, we divided the fault into five segments (labelled S-1 to S-5, Fig. 2) in accord with the field data reported in Xu *et al*. (2006). This subdivision of the fault into five segments will allow us to vary the rupture speed within each segment.

As discussed in Bouchon & Vallée (2003), the seismic station WMQ is located at a backazimuth direction from the epicentre, and the waveform at this station has more distinct arrivals spread out in time. In addition, the velocity structure between the source and the station WMQ is well constrained, as shown in Fig. 10. Thus, we used the waveform recorded at the station WMQ to determine the rupture velocity in each of the five fault segments by fitting the arrival times and amplitudes of the distinct phases of the observed surface wave. The phases corresponding to each fault segment are denoted in Fig. 12(a). For each fault segment, the time window used to determine the delay time between the synthetic and observed waveforms is based on the observed peak pulse that contains the main energy of the rupture. Synthetic waveforms for the first fault segment, S-1, using rupture velocities of 1.3 and 2.4 km s^{-1}, are compared (Fig. 12a). The differences in rupture velocities resulted in the differences in the timing, shape and amplitude of the Love waves. Broader waveforms and later arrival times result from a relatively slow rupture, while a higher rupture velocity produces earlier arrivals with larger amplitudes and narrow waveforms.

Fig. 13 shows the flowchart used in our determination of rupture velocities for each corresponding fault segment. The rupture velocity in each segment was initially set to be 0.8 times the shear wave velocity. For each adjustment of the rupture velocity in the individual segment, the spatial slip distribution was inverted according to the rupture velocities of each fault segment. The modelled surface waves were, thus, synthesized to compare with the observations. Several attempts were made to calculate the rupture velocity in each segment in order to obtain the best fit of the arrival times, wave shape and amplitudes (Fig. 12b). The rupture velocity of

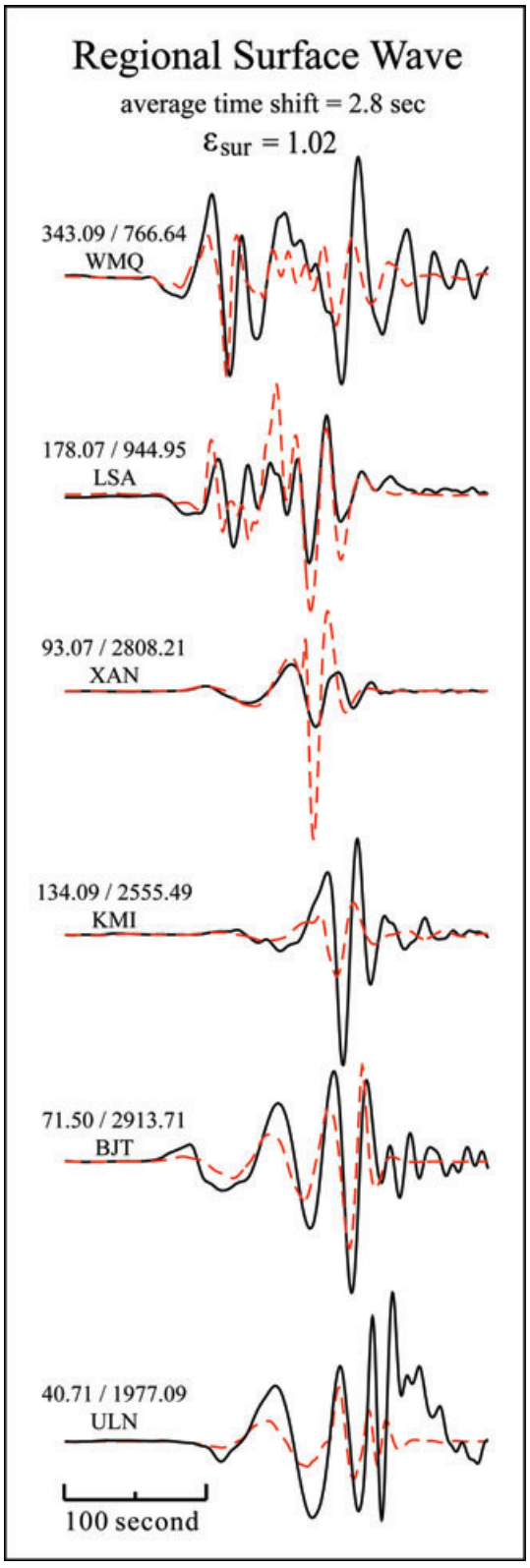

Figure 11. The comparison of the observed (solid line) and synthetic (dashed line) regional surface waveforms for the spatial slip model with a constant rupture velocity of 3.4 km s^{-1} and the geological constraints of Xu *et al*. (2006). The numbers above the station code separated by a slash denote: (1) the station azimuth in degree and (2) peak value of the record in micrometres. All waveforms are shown in absolute amplitude. The observed and synthetic waveforms display clear misfits for this calculation that assumes a constant rupture velocity (3.4 km s^{-1}).

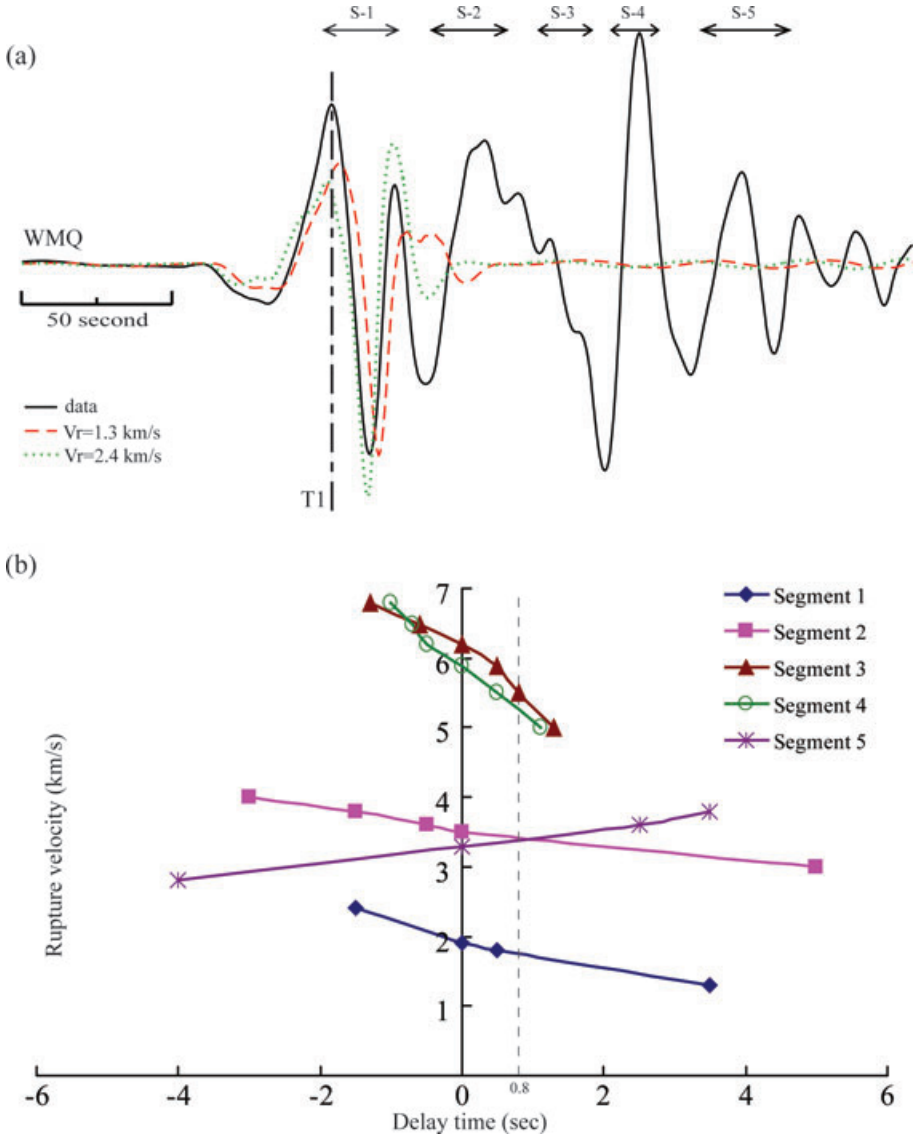

Figure 12. The determination of rupture velocity. (a) The surface waves at the station WMQ (black solid line). The dashed line and dotted line represent the synthetic waveforms for the rupture velocities of 1.3 and 2.4 km s^{-1}, respectively, for the segment S-1. The peak pulse of observed waveform is marked as T1. The time windows for determining the delay time between the synthetics and the observed energy pulse for each fault segment (S-1 to S-5; Fig. 2) are marked above the waveform with horizontal bars. (b) The plot of the rupture velocities and the delay times between synthetics and observed seismograms for each of segments S-1 to S-5. Various rupture velocities (km s^{-1}) were employed in each fault segment as indicated by various symbols. The dashed lines indicate the estimated margin of the error in delay time based on the determination of the refined 1-D velocity structure. Note that segment S-1 has the lowest rupture velocity (1.9 km s^{-1}) and segments S-3 and S-4 have the highest (~6 km s^{-1}).

the each of the five fault segments were determined sequentially by this procedure.

There is an uncertainty in the estimate of rupture velocity due to an imperfect knowledge of the velocity structure, and we use the timing error at the WMQ station (about 0.8 s, Fig. 10) as a way to provide an estimate on the error bounds of rupture velocity for each segment as is shown in Fig. 12(b). The estimated rupture velocities for each segment are: (1) 1.8–1.9 km s^{-1} for S-1; (2) 3.4–3.5 km s^{-1} for S-2; (3) 5.5–6.2 km s^{-1} for S-3; (4) 5.3–5.9 km s^{-1} for S-4 and (5) 3.2–3.3 km s^{-1} for S-5. Thus, our results show that the rupture velocity during the earthquake was initially slow, with a value of about 1.9 km s^{-1}, increased to 3.5 km s^{-1} in the second fault segment (S-2), and then peaked at around 6.0 km s^{-1} (supershear velocity, but not exceeding *P*-wave velocity) in the third and fourth segments (S-3 and S-4). The two segments with a supershear rupture velocity correspond to the locations with the maximum surface offsets reported by Klinger *et al*. (2006) and Xu *et al*. (2006). After rupturing past segment S-4, the rupture velocity decelerated to a value of 3.3 km s^{-1} on the final segment (S-5), although this value is less well resolved. The average rupture velocity over the entire 410 km fault is about 3.6 km s^{-1}. Our result shows similar overall pattern in the variation in rupture velocity as that obtained by Vallée *et al.* (2008) from analysing the high frequency energy radiation using a seismic array.

Fig. 14 shows the fault slip distribution obtained with the additional constraints provided by modelling regional surface waves. This slip distribution synthesizes the teleseismic body waveforms just as well as previous models that were determined without modelling the regional surface waves. However, considering the modelling of regional surface waveforms with varying rupture velocity,

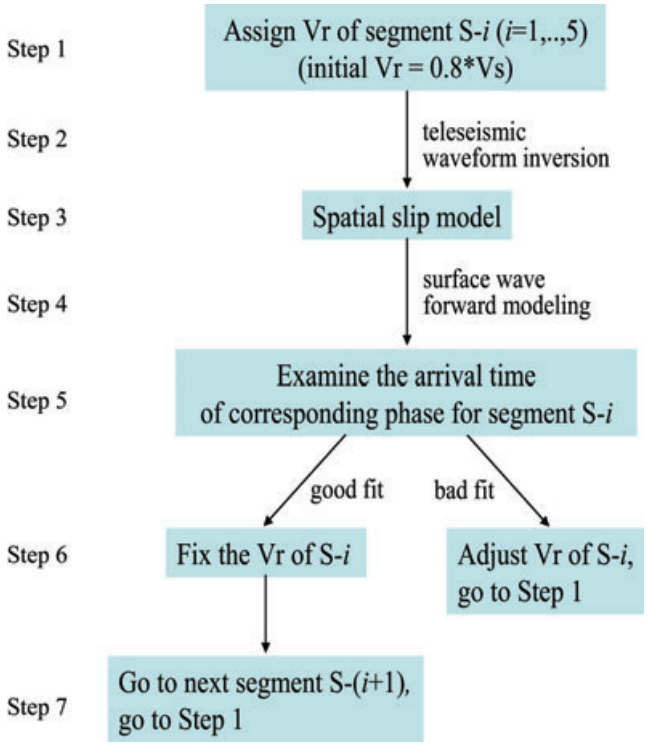

Figure 13. The flowchart shows the procedure for the determination of rupture velocities for each of the corresponding fault segments, S-1 to S-5. The estimated rupture velocities can be seen in Fig. 12.

the synthetic waveforms now explain the amplitudes and timings of the observed waveforms quite well, with the error estimate, $\boldsymbol{\varepsilon}_{\mathrm{sur}}$ decreasing from 1.02 (Fig. 11) to 0.52. The average time shift between the data and synthetics also decreases from 2.8 s (Fig. 11) to 0.9 s. The seismic station LSA, which lies nearly in the perpendicular direction of the ruptured fault, also reveals a wide-angle variation in waveforms, similar to station WMQ. The good fit of the synthetics for station LSA confirms the reliability of the rupture velocities determined from the station WMQ. The waveforms at stations that lie in the forward direction of rupture propagation (XAN, KMI, BJT and ULN) are also fit by our synthetic waveforms quite well. This demonstrates that variations in rupture velocity along the entire 410 km fault are well manifested well in the regional surface waves.

The spatial slip model derived here shows significant composite slips consisting of strike-slip motion with a normal component. This corresponds to the result of Van Der Woerd *et al*. (2002a), Klinger *et al*. (2005) and King *et al*. (2005), where slip-partitioned fault breaks along the Kusaihu subsection (S-3 segment) were observed. Most of the slip is concentrated within a shallow depth (0–10 km) with a small amount of slip extending to a depth of 30 km in some regions where aftershocks occurred (Fig. 1).

4 DISCUSSION AND CONCLUSION

The 2001 Kunlun earthquake produced surface ruptures that total at least 410 km in length (Xu *et al*. 2006), the longest yet observed in the world (Yeats *et al*. 1997). The surface ruptures show significant along-strike variations (Lin *et al*. 2002, 2003; Xu *et al*. 2002, 2006; Lasserre *et al*. 2005; Klinger *et al*. 2005, 2006). Although the main, eastern 350-km-long rupture was remarkably linear in map view, both field observations and teleseismic waveforms suggested complexity in the slip distribution along the fault. Using geological observations as a constraint, we first derived the spatial slip distribution from teleseismic data, and then estimated spatial variations of the rupture velocity using regional surface wave data. Our study highlights the difficulty of using teleseismic waveforms for the determination of variations in rupture velocity. The fault rupture extended 30 km west and about 380 km east of the epicentre. The initial rupture of the 2001 Kunlun earthquake was almost purely strike slip with a rupture velocity of 1.9 km s^{-1}. The earthquake ruptured to the east, and cut through the Taiyang Lake with an oblique normal-faulting mechanism, then returned to left-lateral strike-slip motion over the remainder of the fault. Fault slip was concentrated between the surface and a depth of 10 km. Only about 20 per cent of the moment was released at a depth greater than 25 km. The maximum displacement of 7.8 m occurred about 260 km east of the epicentre. The vertical displacement along the rupture surface was much smaller than the horizontal slip component at all locations. The total seismic moment is 5.35×10^{20} Nm ($M_{\mathrm{w}} = 7.8$).

Fault segment S-3, with a supershear rupture velocity ($\sim$6.0 km s^{-1}) is the region where the fault sub-divides and spreads to a width of 2 km (Klinger *et al*. 2005; King *et al*. 2005). In fault segment S-4, a maximum fault zone width of 8 km was measured (Xu *et al*. 2006), and a rupture velocity of close to 6.0 km s^{-1} was attained. The maximum surface slip was also reported for segment S-4. These comparisons suggest the correlation of high rupture velocity and high fault slip with the formation of the fault breaks or other geometric variations. Bhat *et al*. (2007) showed that off-fault damage is controlled by the speed of the slip-pulse, scaled stress drop and principal stress orientation of the pre-stress field. According to their study, extension-like features were observed a few kilometres away from the Kunlun fault during the 2001 Kunlun event. Bernard & Baumont (2005) pointed out that the ground acceleration due to a supershear rupture is unusually high, creating a broader fault damage zone of a few dozen kilometres. These oberservations are consistent with our results for the two fault segments S-3 and S-4, for which we find the broad fault zone reaching a supershear rupture velocity of about 6 km s^{-1}. Moreover, our model shows significant composite slip consisting of strike-slip motion with a normal component, which corresponds to the slip-partitioned fault along the Kusaihu subsection (S-3 segment). Kanamori & Rivera (2006) suggest that most energy propagates at the velocity of shear waves for shear faults, but that a small amount of energy can propagate at *P*-wave speed for certain geometries. They suggest that the fracture at the crack tip is expected to occur immediately after the arrival of the stress wave caused by slip if there is no resistance or energy dissipation other than interface friction. In addition, Rosakis (2002) suggests that the rupture velocity depends on the available energy per unit crack advance within the supershear regime. This energy attains a maximum value at speeds closer to $\sqrt{2}c_S$ for strong interfaces and reaches c_P for weaker interfaces. Xia *et al*. (2004) also find similar phenomenon from laboratory experiments. Vallée *et al.* (2008) suggests that, in accord with Rousseau & Rosakis (2003) and Bhat *et al.* (2004), the azimuth change at the beginning of the slip-partitioned break modified the stress of the fault. They propose that the supershear regime was driven by the combined effects of the well-established rupture, the geometrical complexity, and the favourable modification of the stress. The significant variation of the rupture speed and observed fault breaks suggest that there are variations in the strength of the interface along the Kunlun fault, which are related to the fault geometry and strength of the crust.

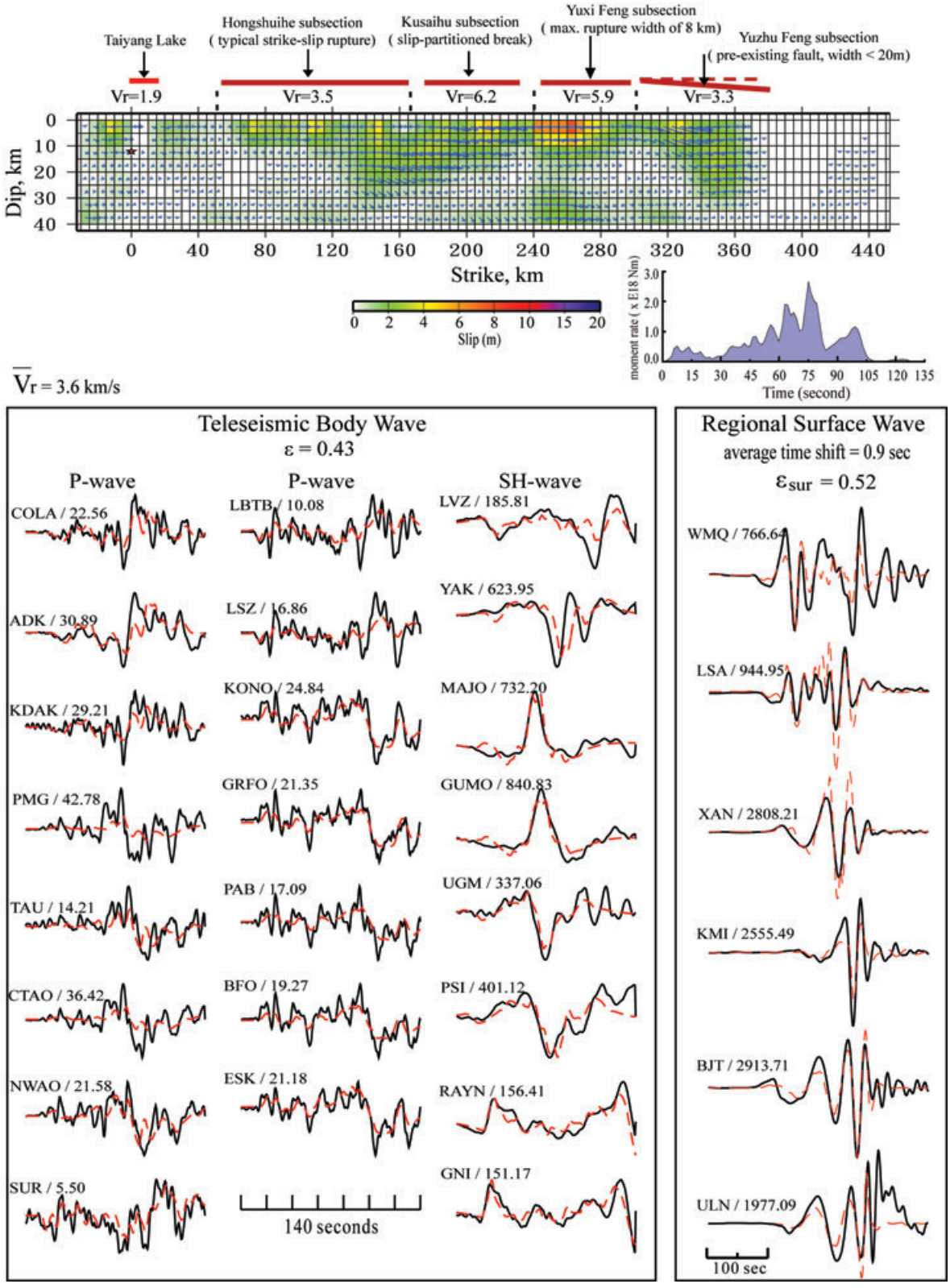

Figure 14. Final slip model that provides the best fit to teleseismic body waves, regional surface waves and the geological field observations of slip. The slip distribution is first estimated by inverting the teleseismic body waves and then is validated by modelling the regional surface waves. The surface slip offsets measured by Xu *et al*. (2006) is used to constrain the inversion. The amount of slip is shown by colour bars in metres. The asterisk indicates the hypocentre location. The arrow indicates the slip vector on the rupture plane. The station name and peak value of the record in micrometres are shown above the waveforms. $\bar{V}r$ indicates the average rupture velocity. The observed geological slip characteristics from Xu *et al*. (2006) are also denoted above the spatial slip distribution for reference. The moment rate function and the synthetics (dashed line) of the teleseismic waveforms and forward modelling regional surface waveforms are shown in comparison to the observations (solid line).

Our study validates this rupture characteristic along the 400-km-long Kunlun fault in a more comprehensive way by integrating the available teleseimic and regional seismic data with geodesy and geological data. Based on these results, it is also possible for us to present an apparent correlation between the region with high rupture speed and the wide damage zone observed in the field. The iterated approach could be applied to other events with similar faulting conditions, such as the 2002 Denali earthquake or the one with unilateral rupture and strike-slip motion.

ACKNOWLEDGMENTS

We appreciate the help and discussion from Xiwei Xu and Jin Zhang at Institute of Geology, China Earthquake Administration, Beijing, China to improve this manuscript. The manuscript was improved by thorough peer reviews of Martin Vallée, an anonymous reviewer, and the editor, Massimo Cocco. This research was supported by the Taiwan Earthquake Center (TEC) funded through National Science Council (NSC97–2745-M-008–013) with TEC contribution number 00018.

REFERENCES

Antolik, M., Abercrombie, R.E. & Ekstrom, G., 2004. The 14 November 2001 Kokoxili (Kunlun Shan), Tibet, earthquake: rupture transfer through a large extensional step-over, *Bull. seism. Soc. Am.,* **94,** 1173–1194.

Bernard, P. & Baumont, D., 2005. Shear Mach wave characterization for kinematic fault rupture models with constant supershear rupture velocity, *Geophys. J. Int.,* **162,** 431–447.

Bhat, H.S., Dmowska, R., Rice, J.R. & Kame, N., 2004. Dynamic slip transfer from the Denali to Totschunda Faults, Alaska: testing theory for fault branching, *Bull. seism. Soc. Am.,* **94,** S202-S213.

Bhat, H. S., Dmowska, R., King, G.C.P., Klinger, Y. & Rice, J.R., 2007. Off-fault damage patterns due to supershear ruptures with application to the 2001 Mw 8.1 Kokoxili (Kunlun) Tibet earthquake, *J. geophys. Res.,* **112,** B06301, doi:10.1029/2006JB004425.

Bouchon, M. & Vallée, M., 2003. Observation of long supershear rupture during the magnitude 8.1 Kunlunshan earthquake, *Science,* **301,** 824–826.

Galvé, A., Hirn, A., Mei, J., Gallart, J., Voogd, B. de, Lépine, J.-C., Diaz, J., Youxue, W. & Hui, Q., 2002. Modes of raising northeastern Tibet probed by explosion seismology, *Earth planet. Sci. Lett.,* **203,** 35–43.

Gu, G., Li, T. & Shen, A., 1989. *Catalogue of Chinese Earthquakes (1831 BC-1969 AD),* Science Press, Beijing, China.

Hjorleifsdottir, V., Kanamori, H. & Tromp, J., 2003. Rupture velocity of the 2001 Kunlun, China, event estimated from SEM waveform modeling, *Eos Trans. AGU,* **84**(46), Fall Meet. Suppl., Abstract #S42E-0218.

Kanamori, H. & Rivera, L., 2006. Energy partitioning during an earthquake, in "Earthquakes: radiated Energy and the Physics of Faulting", *Geophysical Monograph Series 170, AGU Chapman Volume,* 3–13, doi:10.1029/170GM03.

King, G., Klinger, Y., Bowman, D. & Tapponnier, P., 2005. Slip partitioned surface breaks for the 2001 Kokoxili earthquake, China (Mw 7.8), *Bull. seism. Soc. Am.,* **95**(2), 731–738.

Klinger, Y., Xu, X., Tapponnier, P., Van Der Woerd, J., Lasserre, C. & King, G., 2005. High-resolution satellite imagery mapping of the surface rupture and slip distribution of the Mw ~7.8, November 14, 2001 Kokoxili earthquake (Kunlun Fault, Northern Tibet, China), *Bull. seism. Soc. Am.,* **95,** 1970–1987, doi:10.1785/0120040233.

Klinger, Y., Michel, R. & King, G.C.P., 2006. Evidence for an earthquake barrier model from Mw7.8 Kokoxili (Tibet) earthquake slip-distribution, *Earth planet. Sci. Lett.,* **242,** 354–364.

Langston, C.L. & Helmberger, D.V., 1975. Aprocedure for modeling shadow dislocation source, *Geophys. J. R. Astron. Soc.,* **42**, 117–130.

Lasserre C., Peltzer, G., Klinger, Y., Van Der Woerd, J. & Tapponnier, P., 2005. Coseismic deformation of the 2001 Mw = 7.8 Kokoxili earthquake in Tibet, measured by synthetic aperture radar interferometry, *J. geophys. Res.,* **110,** B12408, doi:10.1029/2004JB003500.

Li, H., Van Der Woerd, J., Tapponnier, P., Klinger, Y., Qi, X., Yang, J. & Zhu, Y., 2005. Slip rate on the Kunlun Fault at Hongshui Gou, and recurrence time of great earthquake events comparable to the 14/11/2001, Mw~7.9 Kokoxili earthquake, *Earth planet. Sci. Lett.,* **237,** 285–299.

Li, S.L., Mooney, W.D. & Fan, J.C., 2006, Crustal structure of mainland China frm deep seismic sounding data, *Tectonophysics,* **420**, 239–252.

Lin, A., Fu, B., Guo, J., Zeng, Q., Dang, G., He, W. & Zhao, Y., 2002. Co-seismic strike-slip and rupture length produced by the 2001 Ms 8.1 Central Kunlun earthquake, *Science,* **296,** 2015–2017.

Lin, A., Kikuchi, M. & Fu, B., 2003. Rupture segmentation and process of the 2001 M_w 7.8 Central Kunlun, China, Earthquake, *Bull. seism. Soc. Am.,* **93,** 2477–2492.

Meyer, B., Tapponnier, P., Bourjot, L., Métivier, F., Gaudemer, Y., Peltzer, G., Guo, S. & Chen, Z., 1998. Mechanisms of active crustal thickening in Gansu-Qinghai, and oblique, strike-slip controlled, northeastward growth of the Tibet plateau, *Geophys. J. Int.,* **135,** 1–47.

Molnar, P. & Deng, Q., 1984. Faulting associated with large earthquakes and the average rate of deformation in central and eastern Asia, *J. geophys. Res.,* **89,** 6203–6227.

Ozacar, A.A. & Beck, S.L., 2004. The 2002 Denali Fault and 2001 Kunlun Fault earthquakes: complex rupture processes of two large strike-slip events, *Bull. seism. Soc. Am.,* **94,** S278-S292.

Robinson, D.P., Brough, C. & Das, S., 2006. The Mw 7.8, 2001 Kunlunshan earthquake: extreme rupture speed variability and effect of fault geometry, *J. geophys. Res.,* **111,** B08303, doi:10.1029/2005JB004137.

Rosakis, A.J., 2002. Intersonic shear cracks and fault ruptures, *Adv. Phys.,* **51,** 1189–1257.

Rousseau, C.-E. & Rosakis, A.J., 2003. On the influence of fault bends on the growth of sub-Rayleigh and intersonic dynamic shear ruptures, *J. geophys. Res.,* **108,** 2411, doi:10.1029/2002JB002310.

Tapponnier, P. & Molnar, P., 1997. Active faulting and tectonics in China, *J. geophys. Res.,* **82**(20), 2905–2930.

Tapponnier, P., Xu, Z., Roger, F., Meyer, B., Arnaud, N., Wittlinger, G. & Yang, J., 2001. Oblique stepwise rise and growth of the Tibet plateau, *Science,* **294,** 1671–1677.

Tocheport, A., Rivera, L. & Van Der Woerd, J., 2006. A study of the November 2001 Kokoxili Earthquake: history and geometry of the rupture from teleseismic data and field observations, *Bull. seism. Soc. Am.,* **96,** 1729–174.

Vallée, M., Landès, M., Shapiro, N.M. & Klinger, Y., 2008. The 14 November 2001 Kokoxili (Tibet) earthquake: high-frequency seismic radiation originating from the transitions between sub-Rayleigh and supershear rupture velocity regimes, *J. geophys. Res.,* **113,** B07305, doi:10.1029/2007JB005520.

Van Der Woerd, J., Mériaux, A.S., Klinger, Y., Ryerson, F.J., Gaudemer, Y. & Tapponnier, P., 2002a. The 14 November 2001, Mw = 7.8 Kokoxili Earthquake in Northern Tibet (Qinghai Province, China), *Seismol. Res. Lett.,* **73,** 125–135.

Van Der Woerd, J. *et al*., 2002b. Uniform Post-Glacial slip-rate along the central 600 km of the Kunlun Fault (Tibet), from 26Al, 10Be, and 14C dating of riser offsets, and climatic origin of the regional morphology, *Geophys. J. Int.,* **148,** 356–388.

Vergne, J., Wittlinger, G., Hui, Q., Tapponnier, P., Poupinet, G., Mei, J., Herquel, G. & Paul, A., 2002. Seismic evidence for stepwise thickening of the crust across the NE Tibetan Plateau, *Earth planet. Sci. Lett.,* **203,** 25–33.

Wang, Q. *et al*., 2001. Present-day crustal deformation in China constrained by Global Positioning System measurements, *Science,* **294,** 574–577.

Wittlinger, G. *et al*., 2004. Teleseismic imaging of subducting lithosphere and Moho offsets beneath western Tibet, *Earth planet. Sci. Lett.,* **221,** 117–130.

Xia, K.W., Rosakis, A.J. & Kanamori, H., 2004. Laboratory earthquakes: the sub-Rayleigh-to-supershear rupture transition, *Science,* **303,** 1859–1861.

Xu, X., Chen, W., Ma, W., Yu, G. & Chen, G., 2002. Surface rupture of the Kunlunshan Earthquake (Ms 8.1), Northern Tibetan Plateau, China, *Seismol. Res. Lett.,* **73,** 884–892.

Xu, X., Yu, G., Klinger, Y., Tapponnier, P. & Van Der Woerd, J., 2006. Reevaluation of surface ruion of the 2001 Kunlunshan earthquake (Mw 7.8), northern Tibetan Plateau, China, *J. geophys. Res.,* **111,** B05316, doi:10.1029/2004JB003488.

Yeats, R.S., Sieh, K. & Allen, C.R., 1997. *The Geology of Earthquakes,* Oxford Univ. Press, New York, 568 pp.

Zhu, L. & Rivera, L.A., 2002. A note on the dynamic and static displacements from a point source in multi-layered media, *Geophys. J. Int.,* **148,** 619–627.

Zhao, J.M., Mooney, W.D., Zhang, X.K., Li Z.C., Jin, Z.J. & Okaya, N., 2005. Crustal structure across the Altyn Tagh Range at the northern margin of the Tibetan Plateau and tectonic implications, *Earth planet. Sci. Lett.,* **241,** 804–814.